



**VICTORIA UNIVERSITY**  
MELBOURNE AUSTRALIA

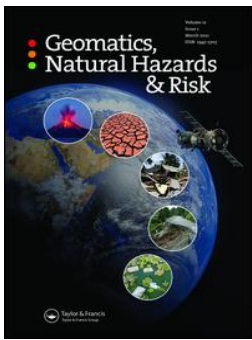
*Time-dependent deformation and fracture evolution  
around underground excavations*

This is the Published version of the following publication

Fu, T-F, Xu, T, Pallewela Liyanage, Piyal wasantha, Yang, TH, Nara, Y and Heng, Z (2020) Time-dependent deformation and fracture evolution around underground excavations. *Geomatics, Natural Hazards and Risk*, 11 (1). pp. 2615-2633. ISSN 1947-5705

The publisher's official version can be found at  
<https://www.tandfonline.com/doi/full/10.1080/19475705.2020.1856202>  
Note that access to this version may require subscription.

Downloaded from VU Research Repository <https://vuir.vu.edu.au/41750/>



## Time-dependent deformation and fracture evolution around underground excavations

Teng-Fei Fu , Tao Xu , P.L.P. Wasantha , Tian-Hong Yang , Yoshitaka Nara & Zhen Heng

To cite this article: Teng-Fei Fu , Tao Xu , P.L.P. Wasantha , Tian-Hong Yang , Yoshitaka Nara & Zhen Heng (2020) Time-dependent deformation and fracture evolution around underground excavations, Geomatics, Natural Hazards and Risk, 11:1, 2615-2633, DOI: [10.1080/19475705.2020.1856202](https://doi.org/10.1080/19475705.2020.1856202)

To link to this article: <https://doi.org/10.1080/19475705.2020.1856202>



© 2020 The Author(s). Published by Informa UK Limited, trading as Taylor & Francis Group.



Published online: 07 Dec 2020.



Submit your article to this journal [↗](#)



Article views: 103



View related articles [↗](#)



View Crossmark data [↗](#)

# Time-dependent deformation and fracture evolution around underground excavations

Teng-Fei Fu<sup>a</sup>, Tao Xu<sup>a</sup> , P.L.P. Wasantha<sup>b</sup>, Tian-Hong Yang<sup>a</sup>, Yoshitaka Nara<sup>c</sup> and Zhen Heng<sup>a</sup>

<sup>a</sup>Center for Rock Instability and Seismicity Research, Northeastern University, Shenyang, China;

<sup>b</sup>College of Engineering and Science, Victoria University, Melbourne, Australia; <sup>c</sup>Department of Civil and Earth Resources Engineering, Graduate School of Engineering, Kyoto University, Kyoto, Japan

## ABSTRACT

A numerical time-dependent deformation model of rock by incorporating the stress corrosion model into a three-dimensional discrete element code was established to investigate time-dependent deformation and fracture evolution of surrounding rock around underground excavations with circular, inverted U-shaped and rectangular cross-sections. The mesoscale model input parameters were calibrated to replicate the mechanical behavior and failure patterns of the rock observed in laboratory. Numerical simulations on the time-independent and -dependent deformation and fracturing evolution of the rock around underground excavations with different shapes under hydrostatic stress were studied. The results show that the maximum time-independent displacements of circular, inverted U-shaped and rectangular openings are 11, 15, and 34 mm at left roof, right floor and left side, respectively. It shows that the surrounding rocks around the circular, inverted U-shaped openings are much more stable than that around the rectangular opening. The cracks within the surrounding rock around different shaped openings gradually increases as time goes by, and the tensile cracks are dominant. The progressive failure process of the circular openings under varying lateral pressures was further modeled. The results show the failure zone at the roof wall and floor wall becomes more evident with an increase in the lateral pressure coefficient.

## ARTICLE HISTORY

Received 7 August 2020

Accepted 22 November 2020

## KEYWORDS

time-dependent deformation; stress corrosion model; fracture evolution; lateral pressure coefficient; underground excavations

## 1. Introduction

Deformation and fracture around underground openings are widely observed, particularly under high and complex in-situ stress (Pan and Dong 1991a; 1991b; Gioda and Cividini 1996; Diederichs 2007; Sterpi and Gioda 2009; Zhao et al. 2010; Gao et al. 2019). The release of stress resulting from the excavation of underground opening disturbs the state of equilibrium of the surrounding rock mass. The excavation

CONTACT Tao Xu  [xutao@mail.neu.edu.cn](mailto:xutao@mail.neu.edu.cn)

© 2020 The Author(s). Published by Informa UK Limited, trading as Taylor & Francis Group.

This is an Open Access article distributed under the terms of the Creative Commons Attribution License (<http://creativecommons.org/licenses/by/4.0/>), which permits unrestricted use, distribution, and reproduction in any medium, provided the original work is properly cited.

boundary acts as the predominant source of stress concentration tangent to the opening in these cases. When the local stress near the tips of the existing flaws exceeds the strength threshold of rock, cracks start to develop from them. Propagation and coalescence of the cracks eventually lead to significant deformation and macroscopic failure around the opening and result in a zone of stress relaxation of the surrounding rock of the opening (Wang et al. 2012; Zuo et al. 2012). After the excavation has been completed, the convergence of the surrounding rock masses may continue to increase as time (e. g., months or years) passes owing to rheological behavior, which greatly affects the determination of the support method for the underground opening (Sulem et al. 1987; Malan 2002; Kontogianni et al. 2006; Xu et al. 2012; Wu and Shao 2019). These observations suggest that a thorough understanding of time-independent and -dependent deformations around an underground opening is essential for their design and construction under in-situ stress condition.

Many previous studies have investigated the deformation and fracturing processes around the underground openings. Germanovich and Dyskin (2000) explain a mechanism of open-hole instability based on the growth of pre-existing micro-fractures in the direction of highest compression. Hajiabdolmajid and Kaiser (2003) proposed a strain-dependent brittleness index ( $I_{Be}$ ) to characterize the brittleness of failing hard rocks and the entire failure process around hard rock tunneling. Zhu et al. (2005) simulated the entire fracturing process around three common shapes of underground excavations under a variety of loading conditions using the realistic failure process analysis (RFPA) code. Lisjak et al. (2014) used a hybrid finite discrete element method (FDEM) to investigate the progressive fracturing mechanisms around different types of underground structures. Fahimifar et al. (2010) proposed an analytical solution to predict the time-dependent displacement and convergence of the circular tunnel, using the Burger's model. Sainoki et al. (2017) employed the Okubo-Fukui model considering the tertiary creep region to investigate long-term tunnel deformation, and demonstrated that the U-shaped tunnel wall closure could take place at an accelerating rate even after a lapse of ten years. Xu et al. (2012) simulated the time-dependent deformation and damage evolution of the circular tunnels under different lateral pressure coefficients using an empirical exponential creep law, and illustrated that the main damage zone was transferred from the sidewalls to the roof and floor of the tunnel with the increase of lateral pressure coefficient.

Either the rheological model or empirical model is often used to study the time-dependent behaviour of rocks (Maranini and Yamaguchi 2001; Shao et al. 2006; Xu et al. 2017; Zhao et al. 2017). The mechanical elements, including spring, dashpot, and slider, are combined in different ways to establish the viscoelastic model or visco-elasto-plastic model (e. g., Maxwell model, Kelvin-Voigt model), characterizing time-dependent deformation of rocks. The empirical models (e.g., the power law, and the hyperbolic law) also successfully describe time-dependent behaviour of rocks. For example, Amitrano and Helmstetter (2006) propose an empirical relation between time to failure and applied stress based on static fatigue laws for the time-dependent deformation and damage of rocks. Time-dependent deformation of the rock mass is mainly attributed to a mechanism of stress corrosion (Das and Scholz 1981; Atkinson 1982; 1984; Atkinson and Meredith 1987). Stress corrosion is driven by reactions that

occur preferentially between a chemically activated geological fluid (commonly water) and the strained bonds at crack tips (Scholz 1972; Michalske and Freiman 1982; Freiman 1984; Baud et al. 2000). Stress corrosion theory was incorporated into the numerical modelling to describe the time-dependent deformation at mesoscale better. For example, Potyondy (2007) introduced stress corrosion into the two- and three-dimensional particle flow code (PFC2D/3D) to mimic time-dependent behaviour in silicate rocks.

This study simulates the progressive fracturing processes around an underground excavation considering both time-independent and time-dependent behaviours at mesoscale (i.e., grain scale). A three-dimensional discrete element grain-based model (3DEC-GBM) was used to represent the surrounding underground rock. The time-dependent behaviour around underground openings with circular, inverted U-shaped and rectangular cross-section were numerically studied by a rheological model using stress corrosion theory under the hydrostatic stress conditions. Deformation and fracturing of the surrounding rock around the circular openings were further analyzed under varying coefficients of lateral pressure.

## 2. Grain-based time-dependent model

3DEC-GBM was built using 3DEC (3-Dimensional Distinct Element Code by Itasca Consulting Group) in this study. It comprised of an assemblage of Voronoi grains with varying shape and size generated in Neper (Quey et al. 2011), which can more reasonably describe the random properties and the internal structure of rock mass, compared with the regular tetrahedron tessellation (Ghazvinian et al. 2014; 2017; Lv et al. 2017; Zhu et al. 2017). For example, the cubic sample shown in Figure 1, comprised of an assemblage of grains of differing shape and size, was built using 3DEC. Each grain in the model is a convex polyhedron (Figure 1) where two adjacent grains share a plane, three adjacent grains share an edge, and four or more adjacent grains share a vertex. 3DEC-GBM allows for an arbitrary displacement and rotation of the grains, as well as a separation of the grains along with their contacts. The rough and undulating fracture pathways can be formed in 3DEC-GBM, along with contacts between grains, and the grain is indivisible (Itasca 2013).

Both grains and grain contacts in the numerical model control the macroscopic behavior of the specimen (Ghazvinian et al. 2014; Muller et al. 2018). The Voronoi grains were assumed to be deformable and made linear elastic without an ultimate strength. The contacts between the deformable grains were assigned the Mohr-Coulomb shear failure criterion and Rankine's maximum tensile stress criterion. The stress corrosion model was further incorporated into 3DEC-GBM to mimic time-dependent response around underground openings at mesoscale, which is the same method of time-dependent deformation presented in Fu et al. (2020). Our implementation of the stress corrosion law was based on the following assumptions: (1) the stress corrosion reaction only occurs at sub-contacts between grains and does not affect the grains; (2) each sub-contact is a potential stress corrosion reaction site at which microcrack forms and propagates; (3) the values of tensile strength and cohesion of the sub-contacts are weakened at the stress corrosion rate. Hence, the

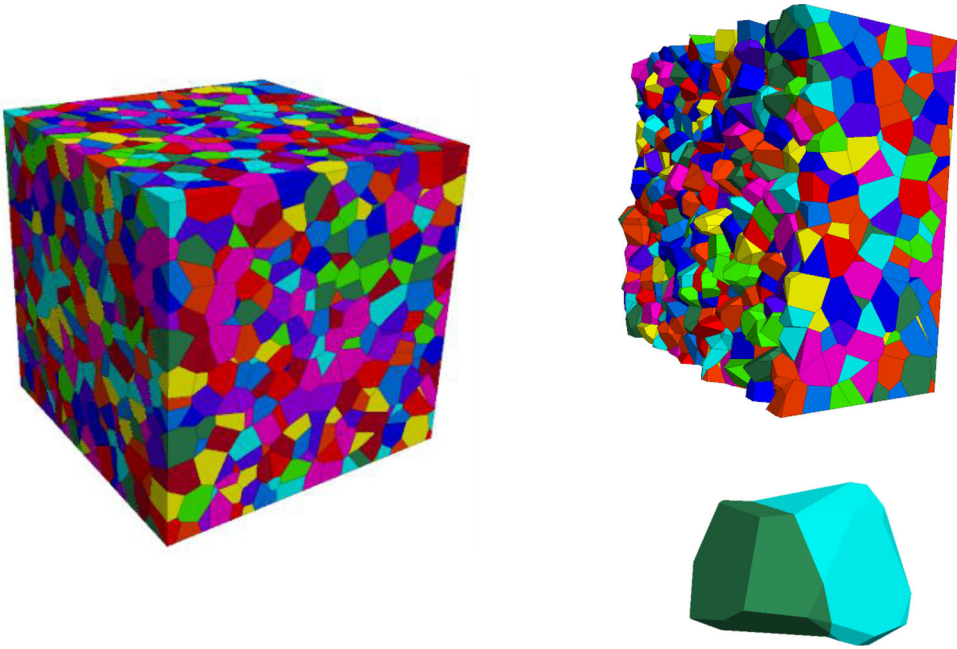


**Figure 1.** A cubic sample showing the polyhedral-shaped elements (left), a section of the cubic sample showing the roughness of an internal surface (potential fracture plane) (right), and a bond between two polyhedral grains (right).

formulation that describes the stress corrosion rate ( $v$ ) of the sub-contacts is given by:

$$v_D = \begin{cases} 0 & \bar{\sigma} < \sigma_0 \\ B_1 e^{B_2 \bar{\sigma}}, & \sigma_0 \leq \bar{\sigma} < \sigma_c \\ \infty & \bar{\sigma} > \sigma_c \end{cases}$$

where  $B_1 = A v_0 e^{-(E^+ + v_M \gamma / \rho) / RT}$  and  $B_2 = v^+ / RT$ ,  $v_0$  is pre-exponential factors,  $v^+$  is the activation volume,  $\sigma$  is the crack-tip tensile stress,  $R$  is the universal gas constant,  $E^+$  is the stress-free activation energy,  $v_M$  is the molar volume of the glass,  $\gamma$  is the interfacial surface energy between the glass and the reaction products,  $T$  is the absolute temperature, and  $\rho$  is the radius of curvature of the crack tip (Atkinson 1984).  $A$  is the constant of proportionality between the chemical reaction rate and the degradation rate,  $\sigma_0$  is the threshold stress (Potyondy 2007),  $\sigma_c$  is the peak strength, and  $\bar{\sigma}$  is the reaction-site stress.

### 3. Model calibration

#### 3.1. Model set-up

We generated a numerical model with a simple geometry of  $20 \times 20 \times 7 \text{ m}^3$  to investigate the fracture evolution around an underground opening caused by excavation. The model consisted of 80,000 Voronoi polyhedron grains, and the equivalent size of

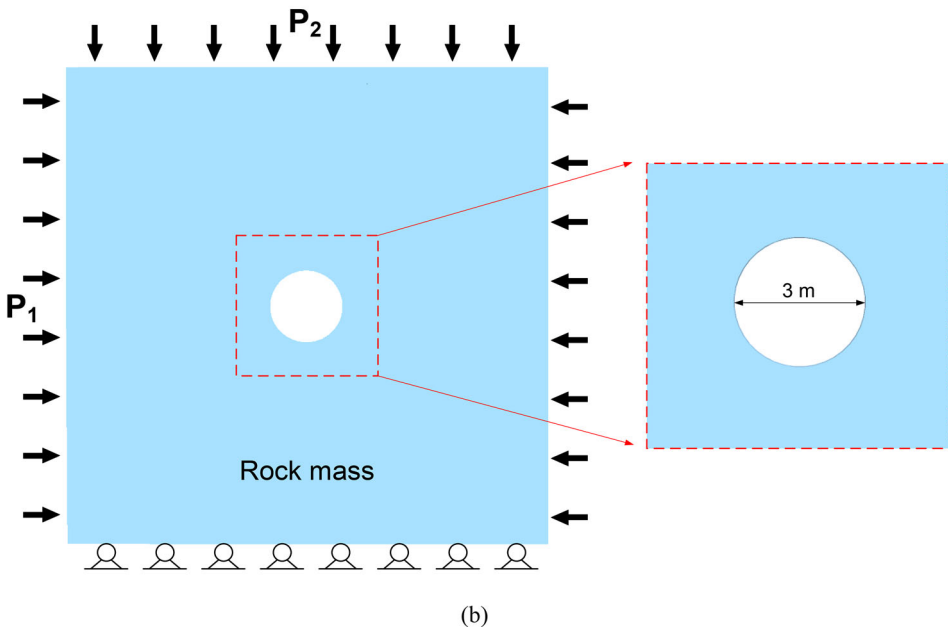
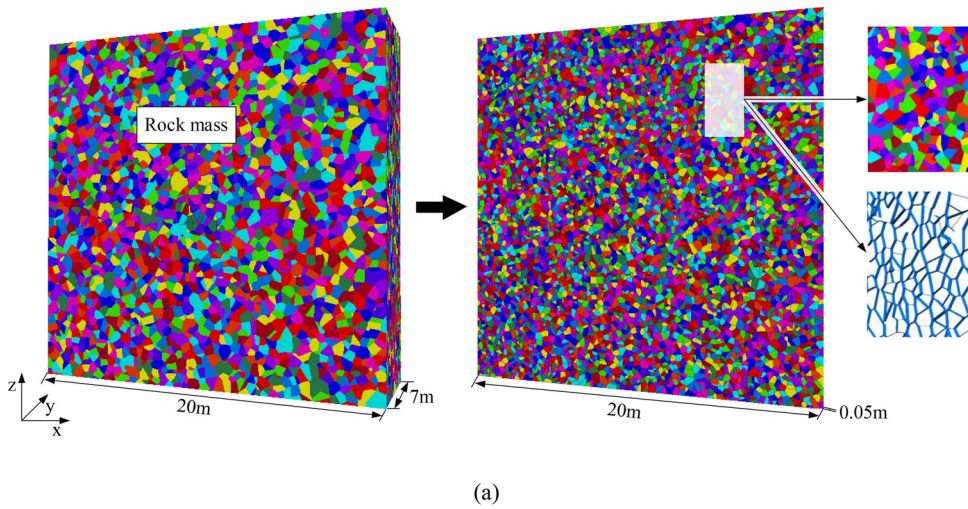
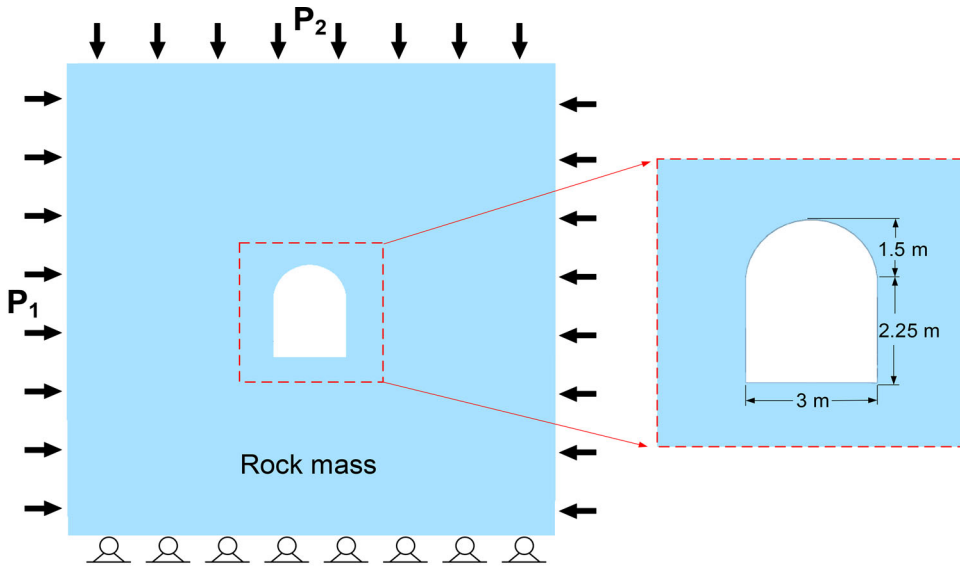
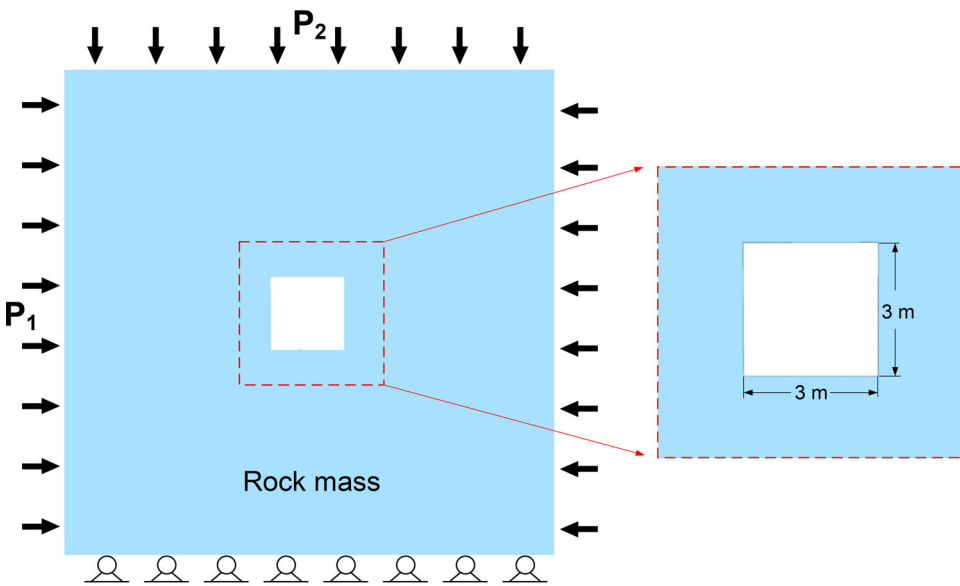


**Figure 2.** (a) Generated the underground opening model (left) and simplified underground opening model with the small thickness (0.05 m) in the Y-direction and zoom-in zone showing grains and contacts (right). (b–d) Numerical model for circular, inverted U-shaped and rectangular openings.

grains was 0.05 m, as shown in Figure 2a. A plane strain condition was considered, and the excavation was simplified to single-stage in order to improve the computational efficiency. Hence, a small thickness (0.05 m) was considered for the model in Y-direction (Figure 2a). As show in Figure 2b–d, three simple geometrical shaped cross-sections of openings, including circular, inverted U-shaped and rectangular, were considered. The height of the rectangular opening and diameter of the circular opening is all 3 m. The height of a straight wall and round arch of the inverted



(c)



(d)

Figure 2. (Continued)

U-shaped opening are 2.25 m and 1.5 m, respectively. The bottom boundary of the opening model is fixed in the Z direction. The horizontal stresses  $P_1$  are applied on the left and right of the model, and the vertical stresses  $P_2$  are applied on the top of the model. The values of  $P_1$  and  $P_2$  all are 40 MPa. The front and back of the model are applied with zero displacement velocity along the Y direction. It should be noted

**Table 1.** The calibrated mesoscale mechanical parameters of the sandstone model.  $E$  – Young’s modulus;  $\nu$  – Poisson’s ratio;  $K_n$  – normal stiffness of the sub-contact;  $K_s$  – shear stiffness of the sub-contact.  $J_T$  – tensile strength of the sub-contact;  $J_c$  – cohesion of the sub-contact;  $\varphi$  – friction angle of the sub-contact;  $\varphi_r$  – residual friction angle of the sub-contact.

$E$ /GPa	$\nu$	$K_n$ /GPa·mm <sup>-1</sup>	$K_n$ / $K_s$	$J_T$ /MPa	$J_c$ /MPa	$\varphi$ /°	$\varphi_r$ /°
12	0.27	40	2	31.2	7.6	27	6

that support systems were not evaluated by the numerical analysis to enable understanding the fracture evolution of surrounding rocks of the underground opening.

### 3.2. Laboratory tests for calibration

We assumed that the surrounding rock of the opening is the intact Yunnan sandstone and no macro-scale discontinuities were considered. The studied Yunnan sandstone was collected in Yunnan, China, and the initial laboratory testing revealed its fundamental properties. The mineralogy of this sandstone is composed of approximately 60% quartz, 19% feldspar, 8% calcite, and 13% cement, and the grain size is approximately 100-200 $\mu$ m. The average density of Yunnan sandstone is 2,119 kg/m<sup>3</sup>, and the average connected porosity, calculated using mercury intrusion porosimetry, is 7.9%. A number of cylindrical specimens of Yunnan sandstone were prepared from a single block, with a diameter of 50 mm and a height of 100 mm. No macroscale defects, such as fractures, were observed in any of these specimens. The uniaxial compression tests were performed on Yunnan sandstone using the 2000 kN capacity TAW testing machine. A constant displacement rate of 0.0025 mm/s, which was equivalent to an axial strain rate of  $2.5 \times 10^{-5} \text{ s}^{-1}$ , was axially loaded on the specimen in compression. The axial deformation was measured directly by three extensometers mounted directly on the specimen. The lateral deformation was measured using a roller-chain circumferential extensometer mounted at mid-height of the specimen. The uniaxial compressive creep tests were also performed by axially loading the specimen at a constant displacement rate of 0.0025 mm/s to a predefined stress level which was held constant until the specimen occurred failure.

### 3.3. Calibration of parameters at a mesoscale

The numerical cylindrical specimens of the same dimension as the laboratory specimens described above in this paper were generated to deform numerically in uniaxial compression and uniaxial compressive creep. The grain elastic constants and contact mesoscale parameters of the numerical specimens were calibrated using a “trial-and-error” method, which has often been used in the literature (Ghazvinian et al. 2014; Gao et al. 2016; Farahmand et al. 2018). A series of numerical simulations (e.g., uniaxial compressive simulation) were performed to find the best design mesoscopic parameter, listed in Table 1, for the studied sandstone. The results show that the numerical model can reproduce the mechanical behavior observed in laboratory experiments. The peak stress and the elastic modulus from the numerical simulation are 52.1 MPa and 11.5 GPa, respectively, which were the same as for the laboratory experiments (Figure 3). A series of numerical creep simulations were further

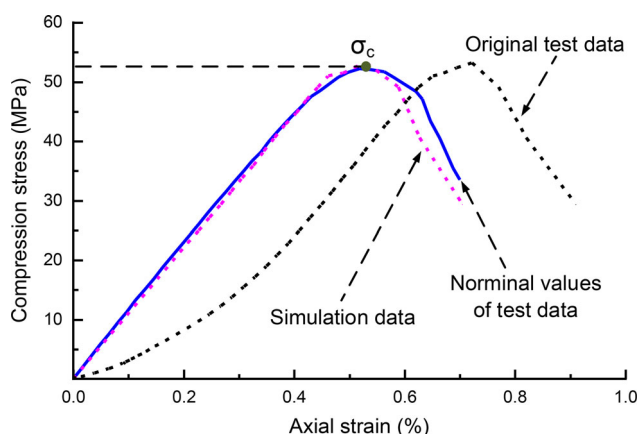


**Figure 3.** Experimental and simulative axial stress-strain curves for a cylindrical laboratory specimen. The solid blue line and dashed red line are experimental and simulative stress-strain curves, respectively. In addition, the dashed pink line is the experimental stress-strain curve with the initial non-linear part of the stress-strain curve removed (Hao et al. 2007). The stresses required for the peak stress ( $\sigma_c$ ) are labeled on the curves.

**Table 2.** Summary of the uniaxial creep simulations at different stress levels.

Short-term failure strength /MPa	Creep stress/MPa	Minimum axial strain rate / $s^{-1}$	Minimum lateral strain rate / $s^{-1}$	Time to failure	
				Simulation/s	Laboratory/s
52.1	36.4	$1.78 \times 10^{-11}$	$3.37 \times 10^{-11}$	$1.36 \times 10^6$	–
	41.6	$2.11 \times 10^{-10}$	$4.51 \times 10^{10}$	$3.14 \times 10^5$	$3.14 \times 10^5$
	44.2	$1.13 \times 10^{-9}$	$3.75 \times 10^{-9}$	$1.15 \times 10^5$	$9.72 \times 10^4$
	46.8	$9.29 \times 10^{-9}$	$2.42 \times 10^{-8}$	$2.92 \times 10^4$	$4.45 \times 10^4$
	49.4	$5.95 \times 10^{-8}$	$1.42 \times 10^{-7}$	$1.70 \times 10^4$	$1.60 \times 10^4$

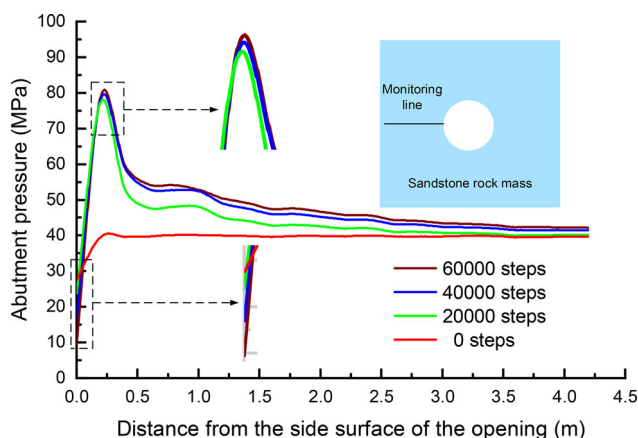


**Figure 4.** Abutment pressure along a monitor line in the left sidewall of the circular opening.

performed based on uniaxial compression creep tests to determine the best design subcritical crack parameters. The values were found to be  $B_1 = 4.3 \times 10^{-4}$  and  $B_2 = 3.5 \times 10^{-7}$ . We found that the model could also capture the time-dependent deformation behaviour of the studied sandstone under different stress level (Table 2).

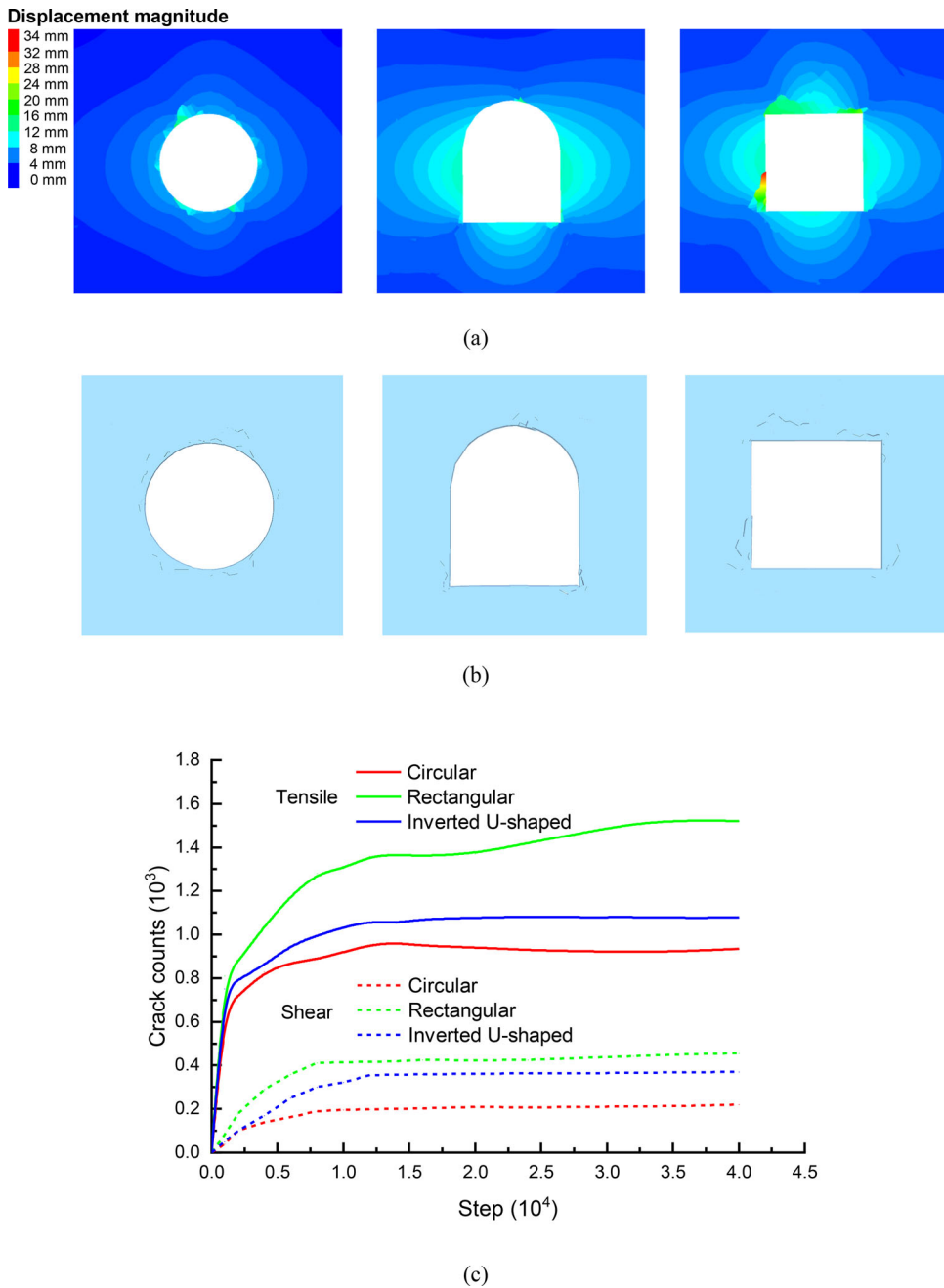


**Figure 5.** Deformation characteristic around the openings with different shaped cross-sections. (a) Simulated displacement vector map; (b) Failure patterns; (c) Crack counts versus step curves.

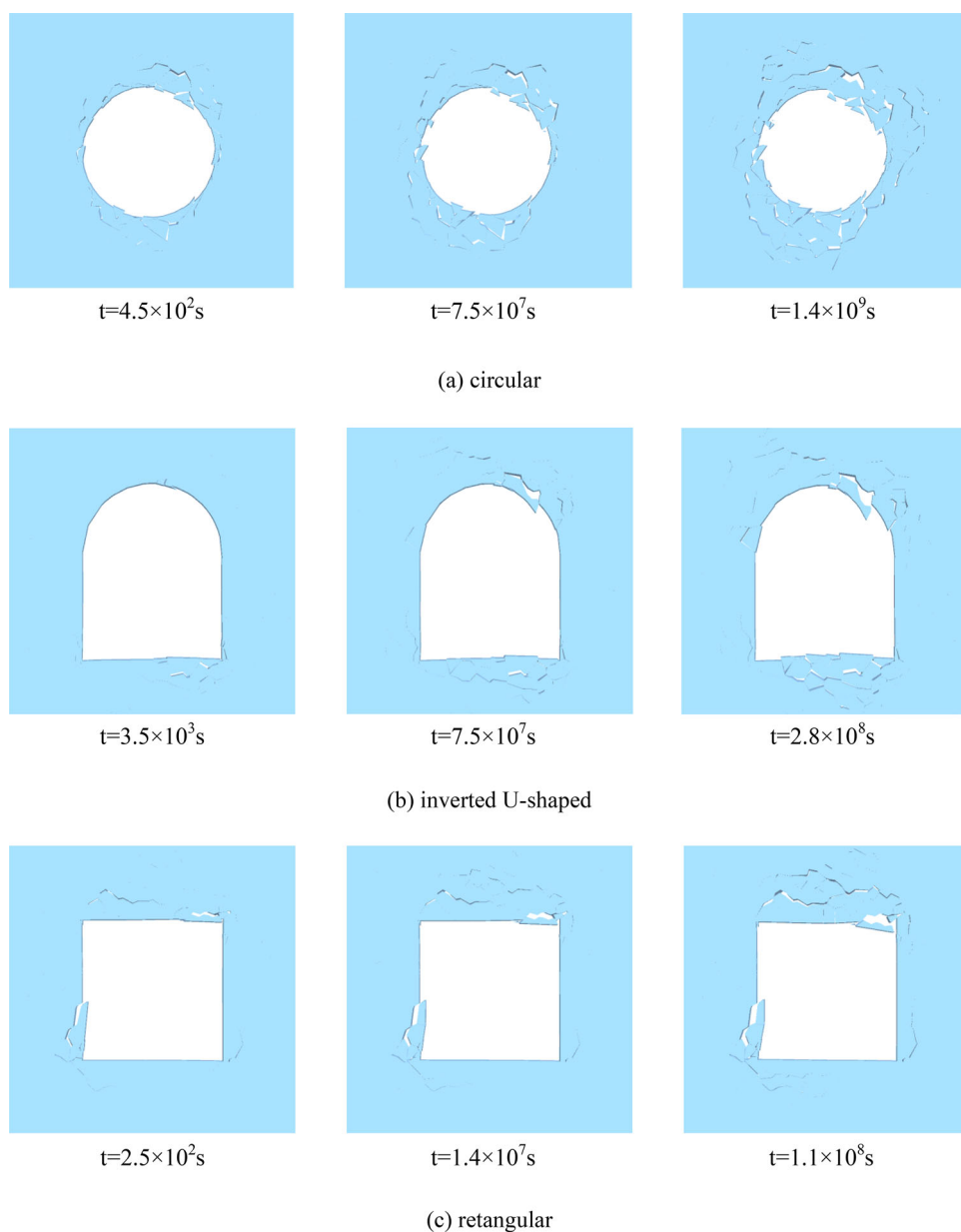


**Figure 6.** Simulated evolutionary process of crack propagation around different shaped openings.

## 4. Modelling deformation and fracturing around underground excavations

### 4.1. Time-independent response of underground openings

The simulated results show that after the underground opening is excavated, stress redistribution occurs in surrounding rock, and stress condition at the opening surface automatically transforms into two-dimension with zero wall-normal stress. The high-stress concentration first appears around the opening surface, and abutment pressure

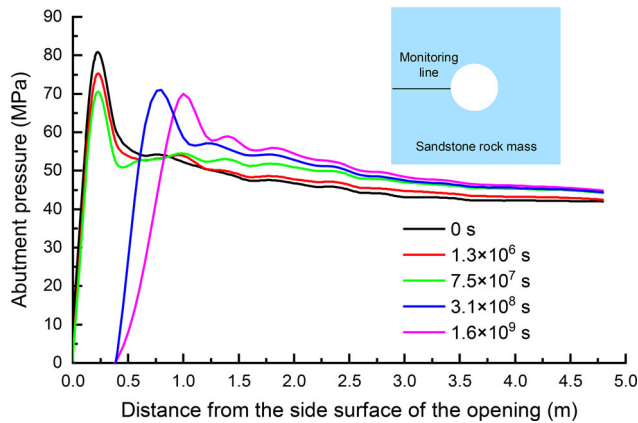
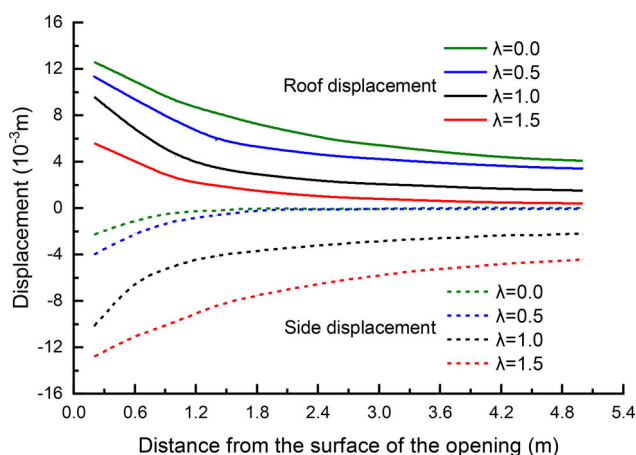


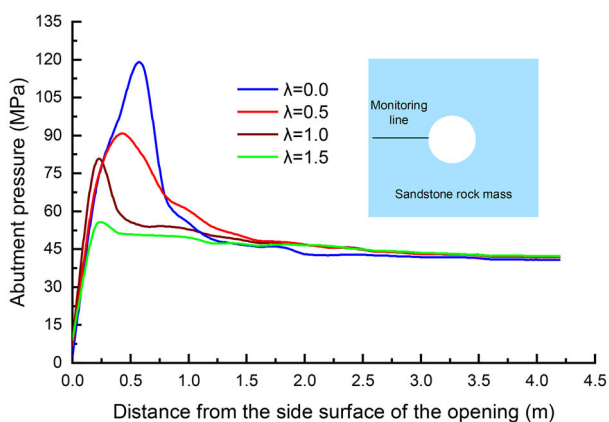
**Figure 7.** Abutment pressure along a monitor line in the left sidewall of the circular opening.

zone is formed within a specific range. When the abutment pressure exceeds the yield strength of surrounding rock, the opening surface enters into a plastic or failure state, and the peak value of abutment pressure transfers to the deep surrounding rock. For example, [Figure 4](#) shows that the abutment pressure near the opening surface is 27 MPa at **20000** steps after the excavation of the circular opening. When the model runs for **60000** steps, the abutment pressure near the opening surface decreases to 13 MPa, and the time-independent deformation is stable. The peak value of abutment pressure is at 0.2 m from the opening surface.

[Figure 5](#) shows simulated displacement vector map and simulated failure patterns of the surrounding rock of the circular, inverted U-shaped and rectangular openings. We observe that the maximum deformation of circular, inverted U-shaped and rectangular opening surfaces appear in the left of the roof, the right of the floor and the left of the side, corresponding on the approximate value of 11 mm, 15 mm, and 34 mm, respectively ([Figure 5a](#)). Deformation in the surrounding rock of the openings is uneven after the excavation, which may be due to the surrounding rock inhomogeneity and the shape of the opening. Moreover, the cross-section shape of openings affects the distribution of fracture location around surrounding rock. For circular opening, the crack propagation randomly occurs anywhere on the surface; for inverted U-shaped opening, the cracks mainly occur in the floor and roof corner around the opening; for rectangular opening, the cracks easily occur in the corner around the opening ([Figure 5b](#)). The formation of cracks within the surrounding rock of different shaped openings increases with timestep. For example, a high rate of the crack formation occurs around the rectangular opening during the initial stage of time-independent deformation ( $< 6500$  steps), afterwards the crack formation rate decreased with timestep. After about **33000** steps, the number of cracks within the surrounding rock is nearly a constant value of 1975 ([Figure 5c](#)). The crack propagation patterns around different shaped openings are similar, and tension cracks are dominant around the openings, accompanied with several shear cracks. For example, the 934 tension cracks, accompanied with 220 shear cracks, are formed within the surrounding rock of the circular opening at **40000** steps ([Figure 5c](#)). The cracks mainly concentrate the surrounding rock near the tunnel surface ([Figure 5b](#)). When



(a)



(b)

**Figure 8.** (a) Displacement along a monitor line in the left sidewall of the circular opening under varying lateral pressure coefficient. (b) Abutment pressure along a monitor line in the left sidewall of the circular opening under varying lateral pressure coefficient.

the time-independent deformation of the surrounding rock of the openings gradually become stable, the number of cracks generated in the circular opening is the least, while the cracks generated in the rectangular opening are the most (Figure 5c). The results demonstrate that the surrounding rocks of the circular and inverted U-shaped openings are much more stable than that of the rectangular opening.

#### 4.2. Fracture evolution of underground openings with time

The evolution of fractures with time around the opening with different shaped cross-sections is shown in Figure 6. We can observe that the fracture zone first appears around the opening surface, and propagates further into the deep surrounding rock.

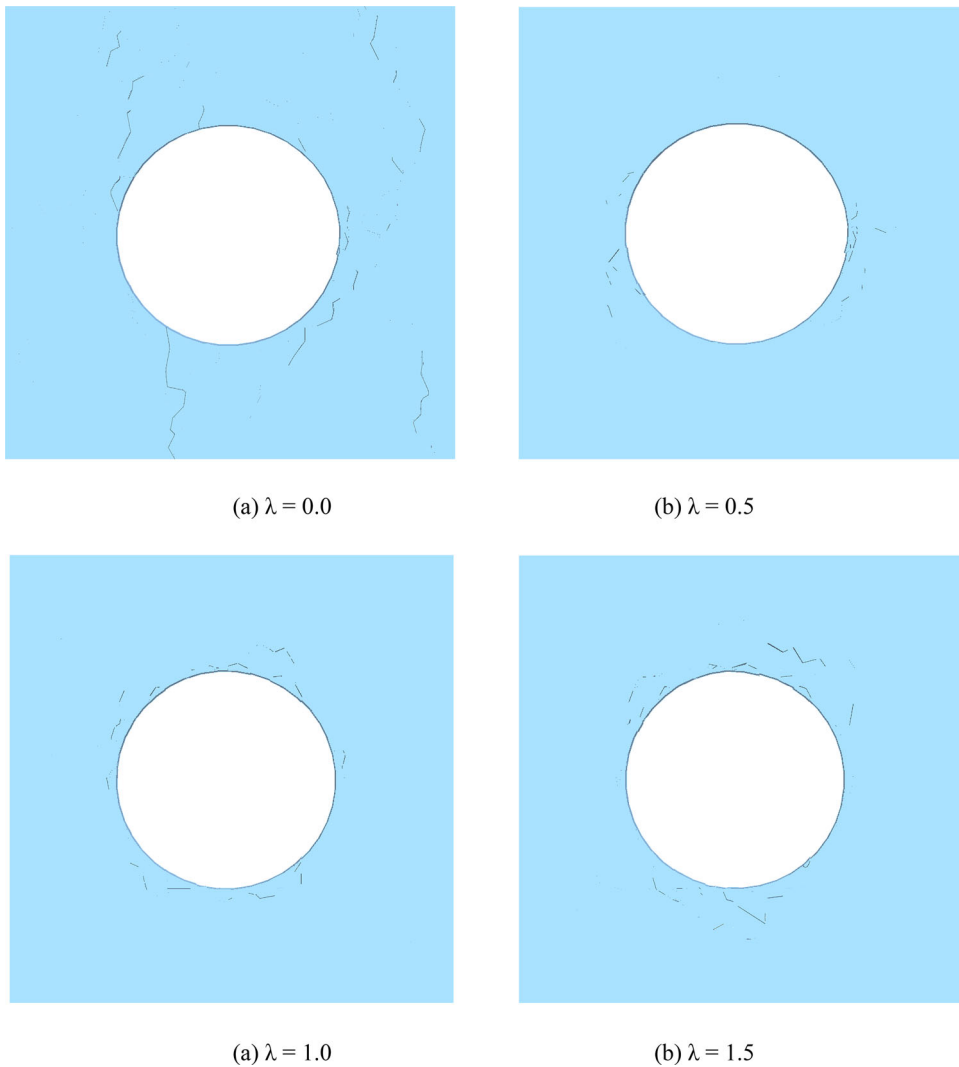


**Figure 9.** Failure patterns around the opening under varying lateral pressure coefficients.

For example, for the inverted U-shaped opening, the failure first concentrates near the opening surface, especially in the roof and floor corner around. The depth of the fracture zone at the floor is 0.62 m and 1.44 m at  $3.5 \times 10^3$  s and  $2.8 \times 10^8$  s, respectively. Correspondingly, the stress concentration also moves into the deeper surrounding rock. For example, as seen in Figure 7, the value of abutment pressure near the left sidewall surface of the circular opening is approximately 6.5 MPa at  $1.3 \times 10^6$  s, taking the maximum value of 76 MPa at 0.25 m from the opening surface. The value of abutment pressure near the left sidewall surface of the opening continues to move downward as time goes by, and it decreases to 0 MPa after a lapse of  $7.5 \times 10^7$  s). Remarkably, after  $3.1 \times 10^8$  s, the value of abutment pressure becomes extremely low in the zone within 0.38 m from the opening surface, forming a broad zone of stress

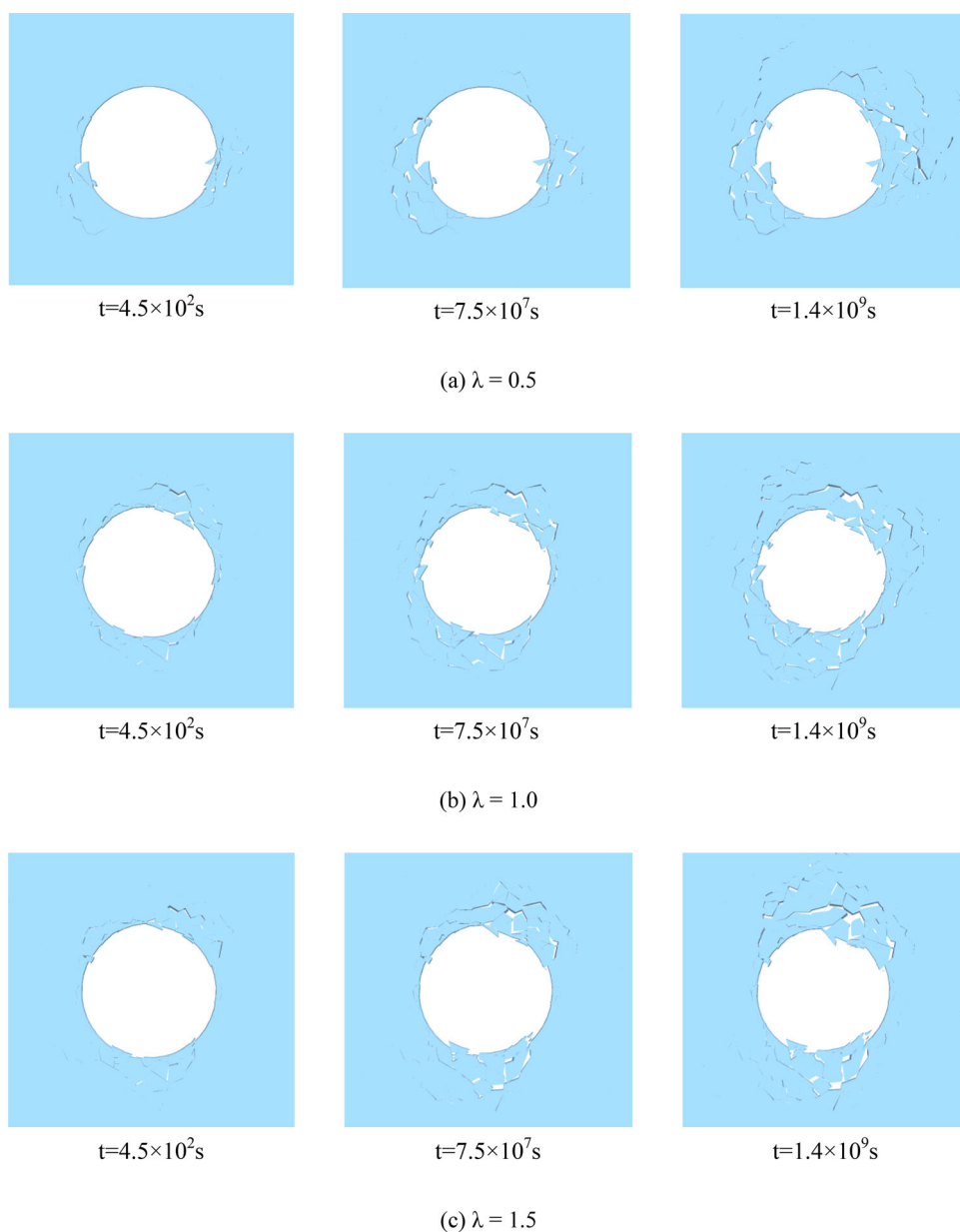


**Figure 10.** Fracture evolution with time around the circular openings under varying lateral pressure coefficients.

relaxation. This demonstrates that it is necessary to support and reinforce the surrounding rock of the openings under this ground stress condition,

### 5. Influence of lateral pressure coefficient on fracture evolution

Time-independent and -dependent deformation of the circular openings were simulated to understand the fracture mechanism around underground openings under

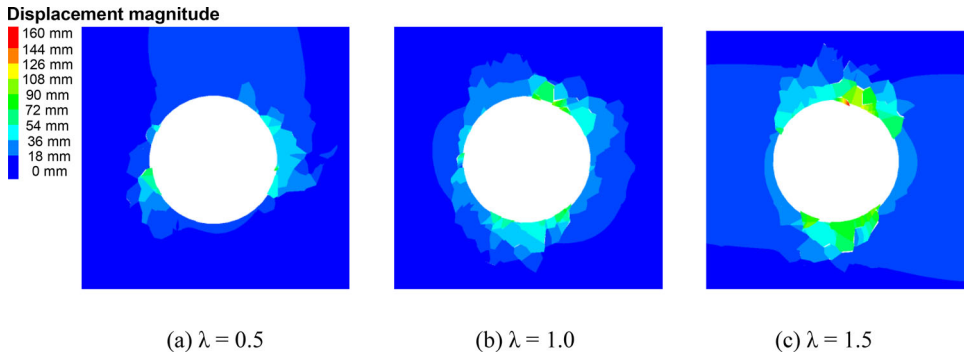


**Figure 11.** Simulated displacement vector map around the circular openings at  $1.4 \times 10^9$  s.

varying lateral pressure coefficients  $\lambda$ . We considered four cases in the model; The vertical stress  $P_2$  was constant at 40 MPa, and the horizontal stresses  $P_1$  were **0, 20, 40** and 60 MPa, corresponding on  $\lambda$  of 0.0, 0.5, 1.0, and 1.5, respectively.

Figure 8 shows the time-independent deformation behavior of the circular opening under varying lateral pressures. With the increase of the lateral pressure coefficient, the displacement of the roof in the opening decreases while that of the side in the opening increases. For instance, the maximum displacements of the roof and the two sides of the opening are 12.5 mm and 2.3 mm, respectively, under the lateral pressure coefficient of 0.5. The maximum displacements of the roof and the left sidewall of the opening are 5.7 mm and 12.8 mm, respectively, under the lateral pressure coefficient of 1.5. The surrounding rock deformation of the opening decreases slowly as increases the distance from the opening surface (Figure 8a). Moreover, when the lateral pressure coefficient increases from 0 to 1.5, the peak value of abutment pressure decreases from 118 MPa to 57 MPa and the distance from the opening surface also decreases from 0.71 m to 0.25 m. When the lateral pressure coefficient is 1.0, the value of abutment pressure along the monitor line approaches in-situ stress at 3.5 m from the opening surface, and the abutment pressure zone is 0.1 ~ 3.5 m from the surface of the opening (Figure 8b).

Figure 9 shows the failure pattern around the circular opening under varying lateral pressure coefficient. We observe that the location of the fracture zone at the roof wall and floor wall becomes more evident as increases the lateral pressure coefficient. For example, fracture zone mainly forms in the sidewall of the circular opening under the lateral pressure coefficient of 0.5, whereas fracture zone mainly concentrates on the roof and floor of the circular opening under the lateral pressure coefficient of 1.5. Moreover, the crack propagation pattern around surrounding rock is similar to the different lateral pressure. Tension cracks are dominant around the opening, accompanied by several shear cracks, and the cracks mainly concentrate near the opening surface (Figure 9). An increase of the lateral pressure coefficient results in the formation of more shear cracks. The ratios of shear cracks to the total number of cracks (i.e., shear and tensile cracks) are 11.9, 17.4, 20.0, and 32.1%, corresponding on lateral pressure coefficients 0.0, 0.5, 1.0, and 1.5, respectively.

The deformation and fracture around the circular openings continue to occur with time after the excavation stability. The evolution of fracturing with ongoing time is

illustrated in Figure 10, in which the failure patterns around the circular opening at  $4.5 \times 10^2$  s,  $7.5 \times 10^7$  s, and  $1.4 \times 10^9$  s are represented. Time-dependent fracture patterns under different lateral pressure are similar to time-independent fracture patterns from Figure 9. For example, when lateral pressure coefficient is 1.5, cracks occur near the opening surface, and more cracks are found closer to the bottom than the two sidewalls of the opening. The primary fracture zone all form in the roof and floor of the opening for both time-dependent and time-independent simulations (Figure 10). We also observe that the fracture zone around the opening gradually expands with time and extends more in-depth into the surrounding rock (Figure 10).

Figure 11 shows the simulated displacement vector map of the surrounding rock of the circular opening at  $1.4 \times 10^9$  s under varying lateral pressure coefficient. The maximum deformation around the opening is directly related to the lateral pressure coefficient. For example, the maximum displacements of the circular openings under the lateral pressure coefficient 0.5 and 1.5 occur in the sidewall and the roof of opening, respectively. The maximum displacements around the opening under the lateral pressure coefficient of 0.5, 1.0, and 1.5 are 81 mm, 104 mm and 160 mm, respectively.

## 6. Conclusions

The mechanical responses of surrounding rock of underground openings after excavation can change with the elapsed time. In this study, we used a three-dimensional discrete element grain-based model (3DEC-GBM) to model the fracture evolution of rock around underground excavations at a mesoscopic scale. The model can reproduce time-independent and -dependent progressive fracture up to failure of the studied sandstone observed in the laboratory. The model can also simulate the time-dependent deformation around underground openings with different shaped cross-section under a variety lateral pressure coefficient. The simulated results show that the deformation around the opening obviously increases after excavation due to the disturbance of the stress equilibrium, and gradually stabilizes. The time-dependent effect within surrounding rock of the opening dominates in the deformation without additional disturbance. The simulated results also show that the surrounding rocks of the arched opening are much more stable than that of the rectangular opening. The displacements around the circular opening are directly related to the lateral pressure coefficients. The established 3DEC-GBM can therefore give a deeper understanding of the fracture evolution around underground excavations at a mesoscale and macroscale. The results discussed in the present study will be great significance to explore the long-term stability of the surrounding rock around the underground openings.

## Disclosure statement

No potential conflict of interest was reported by the authors.

## Funding

The work was jointly supported by National Natural Science Foundation of China (51974062, 41672301, 51950410595), Fundamental Research Funds for the Central Universities of China

(N180101028), National Key Research and Development Program of China (2017YFC1503100).

## ORCID

Tao Xu  <http://orcid.org/0000-0001-8971-674X>

## Data availability statement

The data supporting the findings of this study are available from the corresponding author [T. Xu] on request.

## References

- Amitrano D, Helmstetter A. 2006. Brittle creep, damage, and time to failure in rocks. *J Geophys Res Solid Earth*. 111
- Atkinson BK. 1982. Subcritical crack propagation in rocks: theory, experimental results and applications. *J Struct Geol*. 4(1):41–56.
- Atkinson BK. 1984. Subcritical crack growth in geological materials. *J Geophys Res*. 89(B6):4077–4114.
- Atkinson BK, Meredith PG. 1987. The theory of subcritical crack growth with applications to minerals and rocks. *Fracture Mech Rock*. 2:111–166.
- Baud P, Zhu W, Wong TF. 2000. Failure mode and weakening effect of water on sandstone. *J Geophys Res*. 105(B7):16371–16389.
- Das S, Scholz C. 1981. Theory of time-dependent rupture in the Earth. *J Geophys Res*. 86(B7):6039–6051.
- Diederichs MS. 2007. The 2003 Canadian Geotechnical Colloquium: Mechanistic interpretation and practical application of damage and spalling prediction criteria for deep tunnelling. *Can Geotech J*. 44(9):1082–1116.
- Fahimifar A, Tehrani FM, Hedayat A, Vakilzadeh A. 2010. Analytical solution for the excavation of circular tunnels in a visco-elastic Burger's material under hydrostatic stress field. *Tunnelling Underground Space Technol*. 25(4):297–304.
- Farahmand K, Vazaios I, Diederichs MS, Vlachopoulos N. 2018. Investigating the scale-dependency of the geometrical and mechanical properties of a moderately jointed rock using a synthetic rock mass (SRM) approach. *Comput Geotech*. 95:162–179.
- Freiman S. 1984. Effects of chemical environments on slow crack growth in glasses and ceramics. *J Geophys Res*. 89(B6):4072–4076.
- Fu T, Xu T, Heap MJ, Meredith PG, Mitchell TM. 2020. Mesoscopic time-dependent behavior of rocks based on three-dimensional discrete element grain-based model. *Comput Geotech*. 121:103472.
- Gao FQ, Stead D, Elmo D. 2016. Numerical simulation of microstructure of brittle rock using a grain-breakable distinct element grain-based model. *Comput Geotech*. 78:203–217.
- Gao C, Zhou Z, Yang W, Lin C, Li L, Wang J. 2019. Model test and numerical simulation research of water leakage in operating tunnels passing through intersecting faults. *Tunnelling Underground Space Technol*. 94:103134.
- Germanovich LN, Dyskin AV. 2000. Fracture mechanisms and instability of openings in compression. *Int J Rock Mech Mining Sci*. 37(1-2):263–284.
- Ghazvinian E, Diederichs M, Quey R. 2014. 3D random Voronoi grain-based models for simulation of brittle rock damage and fabric-guided micro-fracturing. *J Rock Mech Geotech Eng*. 6(6):506–521.

- Ghazvinian E, Kalenchuk K, Diederichs M. 2017. Three-dimensional random Voronoi models for simulation of brittle rock damage around underground excavations in laminated ground. *Deep Mining 2017: Eighth International Conference on Deep and High Stress Mining*, Perth, Australia. p. 277–288.
- Gioda G, Cividini A. 1996. Numerical methods for the analysis of tunnel performance in squeezing rocks. *Rock Mech Rock Engng.* 29(4):171–193.
- Hajiabdolmajid V, Kaiser PK. 2003. Brittleness of rock and stability assessment in hard rock tunneling. *Tunnelling Underground Space Technol.* 18(1):35–48.
- Hao SW, Wang HY, Xia MF, Ke FJ, Bai YL. 2007. Relationship between strain localization and catastrophic rupture. *Theor Appl Fract Mech.* 48(1):41–49.
- Itasca 2013. 3DEC, Minneapolis, MN, USA: Itasca Consulting Group Inc.
- Kontogianni V, Psimoulis P, Stiros SC. 2006. What is the contribution of time-dependent deformation in tunnel convergence? *Eng Geol.* 82(4):264–267.
- Lisjak A, Figi D, Grasselli G. 2014. Fracture development around deep underground excavations: Insights from FDEM modelling. *J Rock Mech Geotech Eng.* 6(6):493–505.
- Lv Y, Li H, Zhu X, Liu W. 2017. Discrete element method simulation of random Voronoi grain-based models. *Cluster Comput.* 20(1):335–345.
- Malan DF. 2002. Manuel Rocha Medal Recipient Simulating the Time-dependent Behaviour of Excavations in Hard Rock. *Rock Mech Rock Eng.* 35(4):225–254.
- Maranini E, Yamaguchi T. 2001. A non-associated viscoplastic model for the behaviour of granite in triaxial compression. *Mech Mater.* 33(5):283–293.
- Michalske TA, Freiman SW. 1982. A molecular interpretation of stress corrosion in silica. *Nature.* 295(5849):511–512.
- Muller C, Fruhwirt T, Haase D, Schlegel R, Konietzky H. 2018. Modeling deformation and damage of rock salt using the discrete element method. *Int J Rock Mech Min Sci.* 103: 230–241.
- Pan YW, Dong J. 1991a. Time-dependent tunnel convergence—I. Formulation of the model. *Int J Rock Mech Mining Sci Geomech Abstr.* 28(6):469–475.
- Pan YW, Dong J. 1991b. Time-dependent tunnel convergence—II. Advance rate and tunnel-support interaction. *Int J Rock Mech Mining Sci Geomech.* 28(6):477–488.
- Potyondy DO. 2007. Simulating stress corrosion with a bonded-particle model for rock. *Int J Rock Mech Min Sci.* 44(5):677–691.
- Quey R, Dawson PR, Barbe F. 2011. Large-scale 3D random polycrystals for the finite element method: Generation, meshing and remeshing. *Comput Methods Appl Mech Eng.* 200(17–20):1729–1745.
- Sainoki A, Tabata S, Mitri HS, Fukuda D, Kodama J. 2017. Time-dependent tunnel deformations in homogeneous and heterogeneous weak rock formations. *Comput Geotech.* 92: 186–200.
- Scholz CH. 1972. Static fatigue of quartz. *J Geophys Res.* 77(11):2104–2114.
- Shao J, Chau KT, Feng X. 2006. Modeling of anisotropic damage and creep deformation in brittle rocks. *Int J Rock Mech Min Sci.* 43(4):582–592.
- Sterpi D, Gioda G. 2009. Visco-Plastic Behaviour around Advancing Tunnels in Squeezing Rock. *Rock Mech Rock Eng.* 42(2):319–339.
- Sulem J, Panet M, Guenot A. 1987. Closure analysis in deep tunnels. *Int J Rock Mech Mining Sci Geomech Abstr.* 24(3):145–154.
- Wang S, Sloan SW, Sheng D, Tang CA. 2012. Numerical analysis of the failure process around a circular opening in rock. *Comput Geotech.* 39:8–16.
- Wu K, Shao Z. 2019. Visco-Elastic Analysis on the Effect of Flexible Layer on Mechanical Behavior of Tunnels. *Int J Appl Mechanics.* 11(03):1950027.
- Xu T, Tang C, Zhao J. 2012. Modeling of Rheological Deformation of Inhomogeneous Rock and Associated Time-Dependent Response of Tunnels. *Int J Geomech.* 12(2):147–159.
- Xu T, Zhou G, Heap MJ, Zhu W, Chen C, Baud P. 2017. The Influence of Temperature on Time-Dependent Deformation and Failure in Granite: A Mesoscale Modeling Approach. *Rock Mech Rock Eng.* 50(9):2345–2364.

- Zhao XG, Cai M, Cai M. 2010. Considerations of rock dilation on modeling failure and deformation of hard rocks—a case study of the mine-by test tunnel in Canada. *J Rock Mech Geotech Eng.* 2(4):338–349.
- Zhao Y, Wang Y, Wang W, Wan W, Tang J. 2017. Modeling of non-linear rheological behavior of hard rock using triaxial rheological experiment. *Int J Rock Mech Min Sci.* 93:66–75.
- Zhu W, Liu J, Tang CA, Zhao XD, Brady BH. 2005. Simulation of progressive fracturing processes around underground excavations under biaxial compression. *Tunnelling Underground Space Technol.* 20(3):231–247.
- Zhu D, Tu S, Ma H, Zhang X. 2017. A 3D Voronoi and subdivision model for calibration of rock properties. *Modelling Simul Mater Sci Eng.* 25(8):085005.
- Zuo Y, Xu T, Zhang Y, Zhang Y, Li S, Zhao G, Chen C. 2012. Numerical Study of Zonal Disintegration within a Rock Mass around a Deep Excavated Tunnel. *Int J Geomech.* 12(4): 471–483.